PHILOSOPHICAL MAGAZINE A, 1998, VOL. 77, NO. 5, 1323–1340

Comparison between simulated weak-beam images: application to the extinction criterion in elastically anisotropic crystals

By JOËL DOUIN†, PATRICK VEYSSIÈRE‡ and GEORGES SAADA§

Laboratoire d'Etude des Microstructures, CNRS–Office National d'Etudes et de Recherches Aérospatiales, BP 72, 92322 Châtillon Cedex, France

[*Received 8 July 1997 and accepted in revised form 24 September 1997*]

ABSTRACT

This paper investigates the reasons why the weak-beam contrast of dislocations is largely insensitive to elastic anisotropy. Particular attention is paid to the applicability of the $\mathbf{g}\cdot\mathbf{b}=0$ invisibility criterion for Burgers vector determination to crystals with large elastic anisotropy factors. For this purpose, a method has been designed to allow for a direct comparison between weak-beam images simulated under different $\mathbf{g}\cdot\mathbf{b}$ imaging conditions.

§ 1. INTRODUCTION

The Burgers vector $\mathbf{b}$ of a dislocation is routinely determined by transmission electron microscopy (TEM) based on the diffraction contrast observed under several reflecting vectors $\mathbf{g}$. In elastically isotropic crystals and under two-beam conditions, a screw dislocation becomes invisible when $\mathbf{g}\cdot\mathbf{b}=0$ and this holds true for dislocations comprising an edge component provided the quantity $\mathbf{g}\cdot(\mathbf{b}\times\xi)$, where ξ is a unit vector along the dislocation line, is not too large (Hirsch *et al.* 1965). The so-called $\mathbf{g}\cdot\mathbf{b}=0$ invisibility criterion provides a reasonably simple means to determine the direction of $\mathbf{b}$, which consists in seeking independent reflections under which the defect is out of contrast.

In elastically anisotropic materials imaged under dynamical conditions, the invisibility criterion may not be applicable. Roughly, the more anisotropic the crystal, the more uncertain is the criterion. This difficulty was first pointed out by Head (1967) who showed that under $\mathbf{g}\cdot\mathbf{b}=0$ dynamical conditions in bright field (BF), a screw dislocation in β-CuZn still exhibits significant and complex contrast. Head *et al.* (1973) then designed a technique of image simulation that has proven, and still proves, extremely successful in a number of cases. On the basis of experiments conducted again on β-CuZn, Saka (1984) was the first to draw attention on the fact that the $\mathbf{g}\cdot\mathbf{b}=0$ criterion could also be safely employed in anisotropic materials when observations are conducted under weak-beam conditions, but no explanation for this was provided. Since then, the weak-beam imaging mode has been extensively and successfully applied to a number of anisotropic crystals, such as minerals as well as systems belonging to the rapidly growing field of ordered intermetallic alloys. In

† e-mail: douin@onera.fr.
‡ e-mail: patrickv@onera.fr.
§ e-mail: saada@onera.fr.

some subtle situations of ambiguous contrast properties, to some extent controlled by elastic anisotropy, image simulations must still be performed in order to elucidate possibly artifactual weak-beam observations (Hemker and Mills 1993, Baluc and Schäublin, 1996, Hemker 1997).

The aim of this paper is to investigate the weak-beam contrast of dislocations in an anisotropic crystal by means of computer simulations. A method that enables one to compare reasonably safely between weak-beam contrasts simulated under different imaging conditions is introduced (§ 2) and the validity of the $\mathbf{g} \cdot \mathbf{b} = 0$ criterion checked in the case of β-CuZn (§ 3). Reasons that make the invisibility criterion still applicable under weak-beam conditions in an elastically anisotropic material are examined from a semiquantitative standpoint in § 4.

§ 2. The simulation of dislocation extinction under weak-beam conditions

A dislocation is said to be invisible when its contrast is hardly detectable on the microscope screen or, better, on a plate emulsion. In practice, the identification of an extinction is inherently uncertain and subjective for this depends on imaging conditions (including microscope adjustment and sample properties) as well as on parameters involved in the recording of images (plate sensitivity, exposure time, plate processing, printing conditions, etc.). Moreover, because of the residual contrast which arises when the parameter $\mathbf{g} \cdot (\mathbf{b} \times \xi)$ is large, extinction becomes even more difficult to assess as the dislocation character deviates from pure screw orientation.

Dislocation invisibility is determined relative to the background and this depends upon whether the dislocation is observed under dynamical or kinematical conditions.

(1) Under near-Bragg dynamical conditions, the defect shows as a dark line on a light background both in BF and in dark field (DF) (provided that the foil is thick enough). Since the maximum intensity I_M of the image is located within the undefected region (Hirsch *et al.* 1960, figures 11-4 and 11-5), defect visibility depends on the value of the *intensity minimum* in the defect image, relative to I_M. In practice, defect visibility is only moderately influenced by the recording procedure since most of the intensity originates from the background. Under dynamical conditions, the major source of ambiguity arises from the various sources of residual contrast, that is from the quantity $\mathbf{g} \cdot (\mathbf{b} \times \xi)$ and from elastic anisotropy.

(2) Under weak-beam conditions, diffraction occurs in a volume located in the close vicinity of the defect whose visibility is thus determined by how much the *intensity maximum* emerges from the background. Confusion, if not mistakes, may then occur when plates are underexposed or insufficiently developed. As made clear in the following, further difficulties result from the strong dependence of I_M upon parameters such as the value of the structure factor of the operating reflection $\mathbf{g}$, the $\mathbf{g} \cdot \mathbf{b}$ product and the deviation from the Bragg condition $s_{\mathbf{g}}$ (§ 3).

In practice, the exposure time under dynamical conditions is that given by the exposure meter of the microscope. In the particular case of weak-beam images, however, an additional problem arises from the fact that the dislocation peak represents but a very small fraction of the total surface of the micrograph whose background intensity is by definition very low. Hence, when exposed to the time indicated by the microscope exposure meter, dislocation images are markedly overexposed (a similar difficulty arises for the recording of other highly heterogeneous images, such as diffraction patterns). Accordingly, it is a current experimental procedure to decrease the measured exposure time by a factor between 2.8 and 4 (which represents three to four steps down for the timer of the JEOL 200CX) and to prolong the developing time of the plates far beyond the normal specifications (say 10–15 min in a concentrated developer).

In a given simulated image, the maximum intensity I_M is generally normalized to unity (pixel intensity $C = 1$) and ascribed the white tone while the black tone corresponds to zero intensity ($C = 0$). Hence, defect contrast under weak-beam conditions is artificially set at a maximum regardless of I_M, and this introduces a severe intrinsic limitation in studying extinction based on simulated images (see also § 4.1). This is why the design of a grey scale common to a wide set of images simulated under varied weak-beam imaging conditions is a prerequisite for conducting an unambiguous comparison between them. In addition, the calibration procedure should be flexible enough to account for the fact that, experimentally, one largely compensates for differences in intensity between micrographs, by means of an adequate combination of beam brightness, control of exposure, developing and printing times and, occasionally, appropriate choice of plate sensitivity.

For the comparison between a set of simulated images to be as close as possible to that of real TEM images including situations of invisibility, we have found it most appropriate to mimic the real procedure of plate exposure which, starting from the measurement of an *integrated* intensity, simply consists in assigning an exposure time which the operator adjusts in order to display the feature of interest. For this purpose, we have first ascribed the half-grey tone (e.g. $C_{ref} = 0.5$ within a scale of tones ranging from 0 to 1) to the integrated intensity I_{ref} of a reasonably thick foil (100 nm)† of undefected copper ($\mathbf{g} = 220$ under BF dynamical Bragg conditions at a magnification of 40×10^3). In practice, the exposure time t_{ref} in such conditions is about 1 s. Then, any simulated weak-beam image is ascribed an exposure time related to the calculated integrated intensity by a rule of thumb. The integrated intensity I_{wb} of the weak-beam image thus corresponds to an exposure time of

$$t_{exp} = \frac{t_{ref} I_{ref}}{I_{wb}}, \tag{1}$$

which transforms into

$$t_{wb} = \frac{t_{exp}}{4} \tag{2}$$

when the above-mentioned time compensation required in practice for weak-beam images is accounted for. We have then simulated a [111] screw dislocation in β-CuZn imaged under $\mathbf{g} = 112$, that is under $\mathbf{g} \cdot \mathbf{b} = 2$, and under a moderate deviation from Bragg conditions of $s_{\mathbf{g}} \approx 0.1\,\mathrm{nm}^{-1}$, for the same magnification of 40×10^3. The virtual exposure proposed by the computer (equation (2)) was approximately 16 s, which is reasonable. On the other hand, since exposure times prolonged beyond a realistic duration would invariably reveal very faint image peaks which should in practice remain invisible, the exposure time should be limited to a maximum time

† A reasonable foil thickness is difficult to assess quantitatively. It is always a compromise between many factors including minimizing the blurring effect due to inelastic scattering and increasing the workable length of dislocations.

which we set to 16 s.† The intensity of each image pixel within the common grey scale is given by

$$C_{wb} = \frac{0.5 t_{wb} i_{wb}}{i_{ref}}, \tag{3}$$

where i_{wb} is the intensity calculated at the emergence of a given column of the defected crystal and i_{ref} is that of any column of the reference copper foil.

It should be noted that despite its rudimentary nature the above calibration, which we shall employ in the following to conduct comparative simulations of dislocation contrast under weak-beam conditions (see also § 4.1), is fairly close to the procedure of plate exposure and image printing which one uses in practice.

§ 3. Image simulations

The deviation from Bragg conditions, which determines the intensity of a given beam, can be represented by the deviation parameter $s_{\mathbf{g}}$ or, equivalently, by an oriented length $n\mathbf{g}$ on the systematic row. $s_{\mathbf{g}}$ represents the distance in the reciprocal space between the operating reflection and the Ewald sphere in the direction of the electron beam, while n is the fractional coordinate, in units of $\mathbf{g}$, of the intersection between the Ewald sphere and the systematic row. The notation $\{\alpha\mathbf{g} - n\mathbf{g}\}$ is often employed to indicate that the reflection $\alpha\mathbf{g}$ is operating with the excitation adjusted to $n\mathbf{g}$. Under weak-beam conditions, α is usually set to unity although $\alpha = 2$ is sometimes employed for contrast enhancement (Hemker and Mills 1993, Schäublin and Stadelman 1993, Baluc and Schäublin 1993). $s_{\alpha\mathbf{g}}$ and n are related by

$$s_{\alpha\mathbf{g}} = \frac{(n-1)\lambda(\alpha\mathbf{g})^2}{2}, \tag{4}$$

where λ is the electron wavelength. In the following, we consider that no beams other than those of the systematic row contribute to image formation, as is usually assumed in such simulations.

The present study is restricted to the case of a superdislocation with [111] Burgers vector in β-CuZn (table 1 and figure 1). For simplicity, the dislocation is taken as undissociated. In order to eliminate the further complications brought about by the contribution of the $\mathbf{g}\cdot(\mathbf{b}\times\xi)$ term to the contrast, the present analysis will be restricted to the [111] screw orientation. The images have been generated by means of the Cufour code developed by Schäublin and Stadelmann (1993) which itself originates from the work of Head *et al.* (1973). The fact that the image aspect is little modified upon incorporating extra beams has been reported by Schäublin and Stadelmann (1993) for BF conditions. We have checked that, provided that no diffracted beam is strongly excited, negligible effects, if any, arise from the incorporation of more than two beams in the simulation of weak-beam images. Nevertheless, since computation times of dislocation images are no longer prohibitive (of the order of 1 min), the images presented below were all calculated with six beams, namely $\{-\mathbf{g}, \mathbf{0}, \mathbf{g}, 2\mathbf{g}, 3\mathbf{g}$ and $4\mathbf{g}\}$, where $\mathbf{0}$ represents the transmitted beam. The simulation was run under the column approximation at an operating voltage of 200 kV. In order to reduce further the number of parameters investigated, we have in a first series of

† In fact, this duration of 16 s is the maximum exposure time that ensures drift-free images in a JEOL 200CX electron microscope at the 1 nm resolution which is normally expected under weak-beam coditions.

Table 1. Input parameters used in the simulation of dislocation image (the elastic constants are taken from Lazarus (1948, 1949)).

Alloy	β-CuZn
Foil thickness	100 nm
Acceleration voltage	200 kV
Elastic constants	
c_{11}	129.1 GPa
c_{12}	109.7 GPa
c_{44}	82.4 GPa
A	8.5
Foil normal **FN**	$[031]$ (figures 2, 3 and 5)
Beam direction **B**	$[0\bar{2}\bar{1}]$ (figures 2, 3 and 5)
Foil normal **FN**	$[5\bar{3}1]$ (figure 4)
Beam direction **B**	$[\bar{5}31]$ (figure 4)
Foil normal **FN**	$[5\bar{3}1]$ (figure 10)
Beam direction **B**	$[\bar{1}10]$ (figure 10)
Dislocation line ξ	[111]
Burgers vectors **b**	[111]
Beams	$-\mathbf{g}, \mathbf{0}, \mathbf{g}, 2\mathbf{g}, 3\mathbf{g}, 4\mathbf{g}$ ($\mathbf{g} = \bar{1}\bar{1}2$ and $\mathbf{g} = 11\bar{2}$)
Anomalous absorption coefficients	
α_{112}	0.0709
α_{224}	0.1027
α_{336}	0.0991
α_{448}	0.0643
$\alpha_{5\,5\,10}$	0.0247

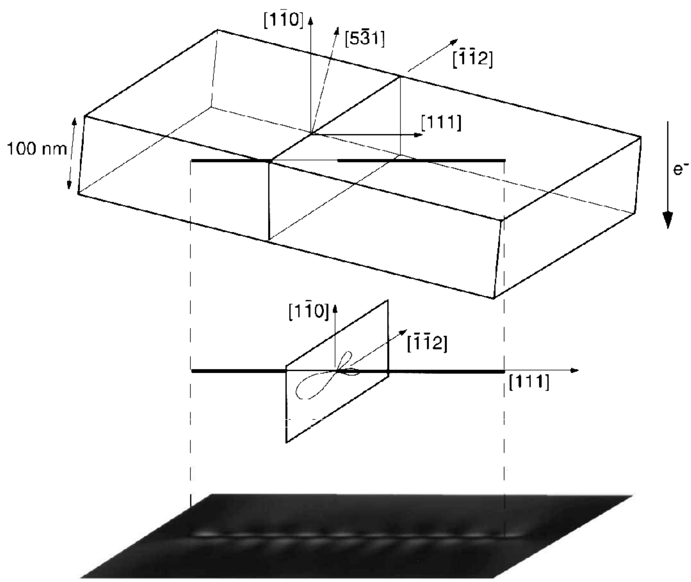

Figure 1. The three elements of interest in the simulations. At the top is the dislocation-containing thin foil whose normal is inclined to the electron beam (here the foil normal and the direction of the electron beam are those used for figures 8, 9 and 10, e.g. $[5\bar{3}1]$ and $[\bar{1}10]$ respectively). The sketch in the middle represents a cross-section of the gradient of $\partial(\mathbf{g}\cdot\mathbf{R})/\partial z$ and the lower image is the simulated image. In every simulation, the projection of the dislocation line on the image is located exactly at half the height of the image.

simulations (figures 2–5) restricted image comparison to reflections with identical structure factors. Amongst the reflections of β-CuZn which have a reasonably strong structure factor, the 112 reflections are the most appropriate for our purpose although the contrast simulated under $\mathbf{g} \cdot \mathbf{b} = 0$ can only be compared then with that under $\mathbf{g} \cdot \mathbf{b} = \pm 2$.

Figure 2 shows a set of four images simulated under $\mathbf{g} = \bar{1}\bar{1}2$ ($\mathbf{g} \cdot \mathbf{b} = 0$), one in the BF mode for $s_\mathbf{g} = 0$ and three in DF mode for increasing values of the deviation

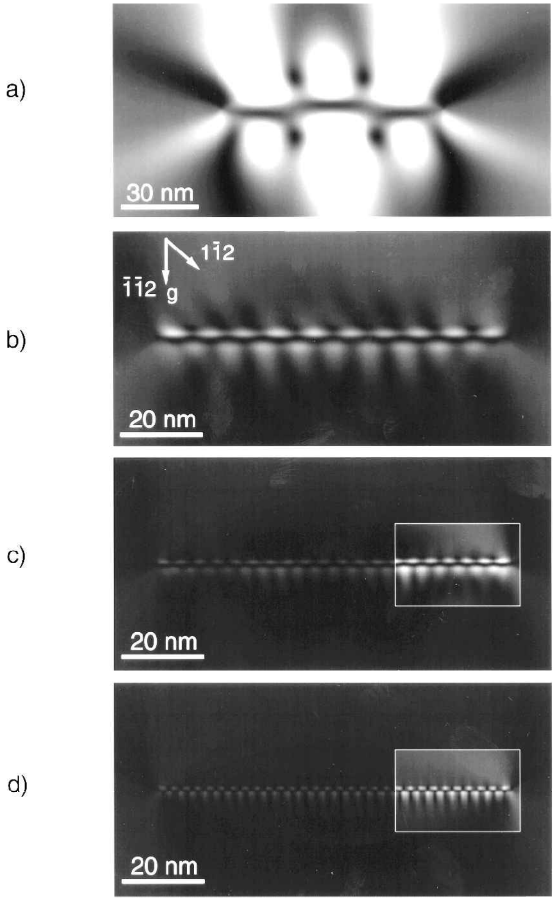

Figure 2. Simulated images of a [111] screw dislocation in β-CuZn under the operating reflection $\mathbf{g} = \bar{1}\bar{1}2$ ($\mathbf{g} \cdot \mathbf{b} = 0$). The data used in the computations are listed in table 1. The calibrated exposure time is 16 s for all images but (*a*). The insets, which are 'exposed' for 90 s, illustrate that, just as in a microscope, all one needs in order to enhance the visibility of the defect is to lengthen the exposure time adequately. (*a*) BF image, $s_\mathbf{g} = 0$. Note the presence of a line of no contrast which corresponds to the position of the projection of the dislocation line (see § 5.3). The line of no contrast is characteristic feature of the morphology of the dislocation image for $\mathbf{g} \cdot \mathbf{b} = 0$, irrespective of $s_\mathbf{g}$. The exposure time is 4 s in this case. In order to show the wholesale morphology of the dislocation image better, the magnification has been reduced relative to that of the DF images in (*b*), (*c*) and (*d*). (*b*) DF image; $s_\mathbf{g} = 0.1\,\mathrm{nm}^{-1}$; the faint peak located on either side of the projection of the dislocation line should be noted. (*c*) DF; $s_\mathbf{g} = 0.2\,\mathrm{nm}^{-1}$. (*d*) DF; $s_\mathbf{g} = 0.3\,\mathrm{nm}^{-1}$. The signal originating from the dislocation is now hardly visible but is in the inset.

parameter s_g of 0.1, 0.2 and 0.3 nm^{-1} (within these it is in fact for $s_g = 0.1$ nm^{-1} that the above calibration yields a calculated exposure time of 16 s, just as for $\mathbf{g}\cdot\mathbf{b} = 2$ (§ 2), which in turn points to the negligible contribution of the dislocation peak to the overall intensity). The simulated image in dynamical conditions exhibits a strong contrast (figure 2(*a*)), as is observed in practice (Head 1967, Saka 1984, G. Dirras 1997, private communication), hence exemplifying the considerable effect of elastic anisotropy on dislocation images. As s_g is increased, the dislocation shows some faint residual contrast for $s_g = 0.1$ nm^{-1}. It becomes invisible in practice for $s_g = 0.2$ nm^{-1}. By comparison, when the $\mathbf{g}\cdot\mathbf{b}$ product is set to 2 the dislocation remains unambiguously visible up to $s_g = 0.3$ nm^{-1} ($\mathbf{g}$–3.3$\mathbf{g}$, (figure 3)). Figure 4 shows that dislocation invisibility does not depend on foil orientation although the contrast for these $\mathbf{g}\cdot\mathbf{b} = 0$ images is a little stronger than in figure 2.

It is worth noting that the simulated images in figure 2 retain a line of no contrast over the entire range of s_g (see § 5.3 and figure 10(*a*)). This gives rise to an unexpected twofold fine structure under weak-beam conditions which wrongly suggests that the dislocation is split to a separation of several nanometres. The persistence of the line of no contrast illustrates the similitude between weak-beam images and the dynamical images simulated under the same reflection. This similitude can be verified in every set of images shown in the present paper. For instance, the weak-beam images

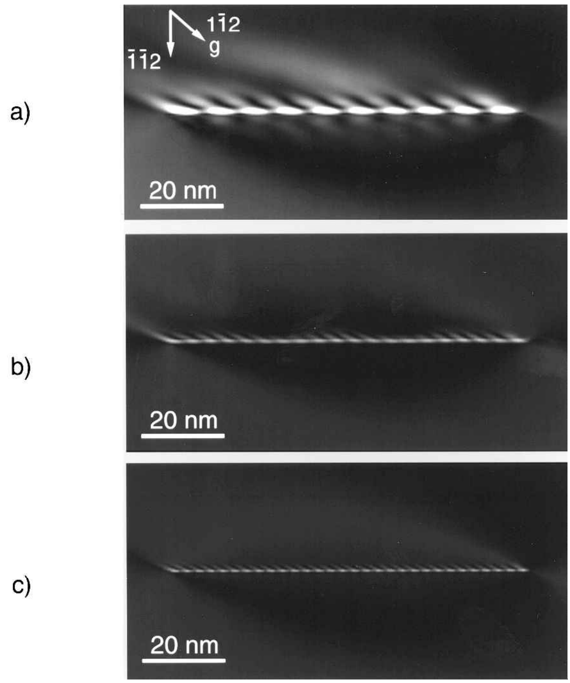

Figure 3. Simulated images of the screw dislocation under $\mathbf{g} = 1\bar{1}2$ ($\mathbf{g}\cdot\mathbf{b} = 2$) for the same crystal orientation as in figure 2. The exposure time calculated for $s_g = 0.1$ nm^{-1} is 16 s, which is the time fixed arbitrarily (§ 2) for the other two images simulated for larger values of s_g. (*a*) DF image; $s_g = 0.1$ nm^{-1}. (*b*) DF; $s_g = 0.2$ nm^{-1}. (*c*) DF; $s_g = 0.3$ nm^{-1}; the dislocation remains strongly visible. Note that, as s_g is increased, the pronounced elongation of the intensity lobes towards the upper left-hand side of the figure shrinks but without disappearing, illustrating the property of similitude of dislocation images as s_g is varied.

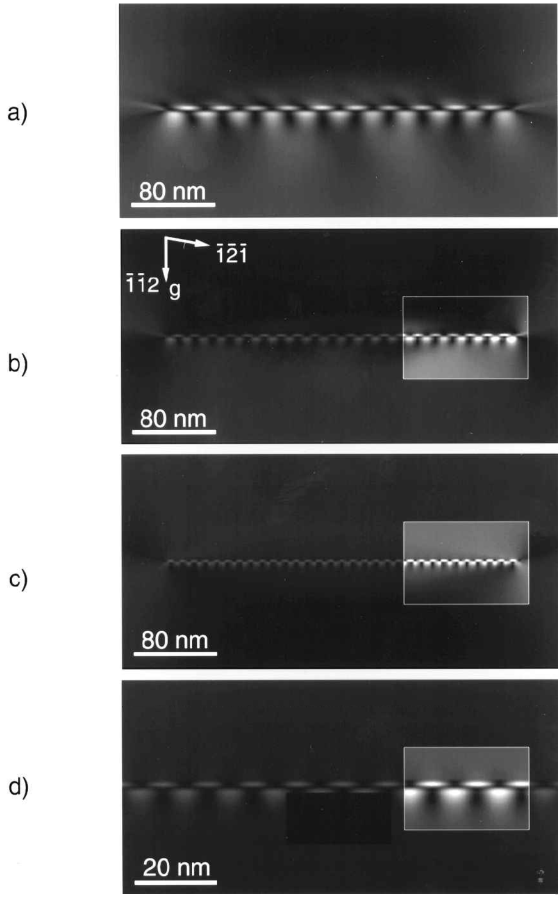

Figure 4. Simulated images under $\mathbf{g} = \bar{1}\bar{1}2$ ($\mathbf{g} \cdot \mathbf{b} = 0$). The foil normal is now along $[5\bar{3}1]$. The geometry of the configuration (figure 1) makes it necessary to display the image under a magnification significantly smaller than that used in the previous weak-beam images. (*a*) DF image; $s_{\mathbf{g}} = 0.1\,\mathrm{nm}^{-1}$. (*b*) DF; $s_{\mathbf{g}} = 0.2\,\mathrm{nm}^{-1}$; the dislocation is nearly invisible. (*c*) DF; $s_{\mathbf{g}} = 0.3\,\mathrm{nm}^{-1}$. (*d*) same as (*c*) but, for comparison, with the same magnification as for figure 2. Insets are exposed for 44 s. Note the presence of a line of no contrast again for this $\mathbf{g} \cdot \mathbf{b} = 0$ condition (see figure 2).

in figure 3 exhibit a succession of oblique streakings which is reminiscent of the image symmetry in dynamical conditions (by contrast, the pseudoperiodicity of the image together with its extension change, as expected). The same remark on similitude holds true for figures 4 and 5 and we shall show in § 4 that this property has its origin in a similitude of the dislocation displacement field.

Given $\mathbf{g}$ and $s_{\mathbf{g}}$, the dependence of dislocation contrast upon foil orientation originates from elastic anisotropy, as demonstrated by the fact that, in an elastically isotropic crystal, imaging under $\mathbf{g} \cdot \mathbf{b} = 0$ yields no contrast at all. In the present case of β-CuZn, the splitting of the image under $\mathbf{g} \cdot \mathbf{b} = 0$ depends on foil orientation; it is less pronounced in the $[5\bar{3}1]$ than in the $[031]$ foil orientation (figures 4 and 2 respectively). The role of anisotropy is further exemplified by comparing between the weak-beam images in figures 3 and 5 whose input data differ only with regards to elastic constants. Those chosen for the simulations of figure 5 correspond to a hypothetically

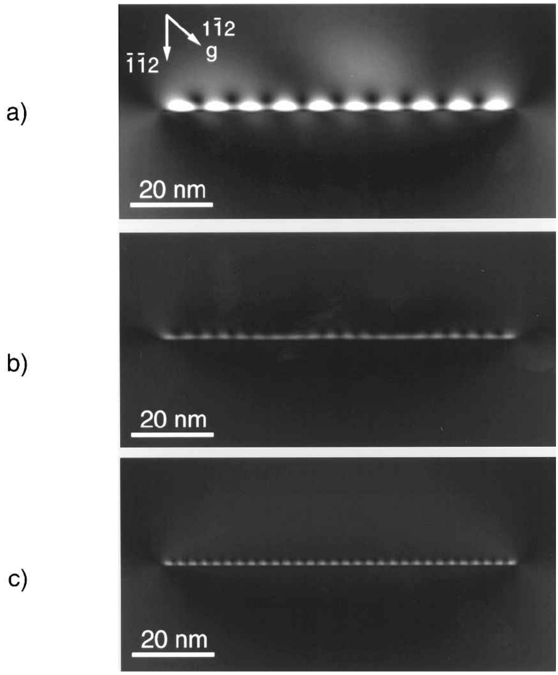

Figure 5. Simulation conducted under $\mathbf{g} = 1\bar{1}2$ ($\mathbf{g} \cdot \mathbf{b} = 2$) of a screw dislocation in a hypothetical crystal whose elastic constants have been adjusted to render the crystal elastically isotropic; with this aim, two elastic constants instead of one have been modified in order to maintain the set of elastic constants within a realistic range of values (c_{11} = 201.8 GPa, c_{12} = 37.0 GPa and c_{44} = 82.4 GPa). (*a*) DF image; $s_\mathbf{g} = 0.1\,\mathrm{nm}^{-1}$. (*b*) DF; $s_\mathbf{g} = 0.2\,\mathrm{nm}^{-1}$. (*c*) DF; $s_\mathbf{g} = 0.3\,\mathrm{nm}^{-1}$. At variance from figure 2, the intensity lobes are no longer elongated towards the upper left-hand side of the images.

isotropic crystal. In the anisotropic crystal, the periodic white lobes are inclined about 30° to the main line (figure 3 (*a*)), while they are not in the isotropic case (figure 5 (*a*)).

§ 4. Contrast similitude

In the presence of a distortion, the portion of crystal which is set in Bragg condition for the reflection $\mathbf{g}$ corresponds to the locus of elementary volumes, called contour maps (Hemker and Mills 1993, Hemker 1997), which satisfy the relation (Cockayne *et al.* 1969)

$$s_\mathbf{g} + \frac{\partial(\mathbf{g} \cdot \mathbf{R})}{\partial z} = 0, \tag{5}$$

where $\mathbf{R}(x, y, z)$ is the displacement field generated by the crystal defect. The dislocation is aligned with the y axis and the electron beam is parallel to the z axis. Equation (5) is equivalent to stating that the deviation from the Bragg condition is compensated locally by the lattice rotation generated by the defect. The expression on the left-hand side of equation (5) represents the effective deviation parameter $s_\mathbf{g}^{\mathrm{eff}}$ in the distorted region (Hirsch *et al.* 1960). Since the strain field $\varepsilon(\mathbf{r})$ of a dislocation is a function of the reciprocal of the distance r from the dislocation, one has

$$\varepsilon(\lambda\mathbf{r}) = \frac{1}{\lambda}\varepsilon(\mathbf{r}); \tag{6}$$

hence

$$\frac{\partial R_k(\lambda x, \lambda z)}{\partial z} = \frac{1}{\lambda}\frac{\partial R_k(x, z)}{\partial z}, \tag{7}$$

When the coordinates x and z are multiplied by λ, the local derivative $\partial \mathbf{R}/\partial z$ and hence the local curvature of the plane $\partial(\mathbf{g}\cdot\mathbf{R})/\partial z$ are multiplied by λ^{-1}. Under anisotropic elasticity, the derivation of equation (7) proceeds exactly in the same way. According to Eshelby *et al.* (1970) the components R_k of the displacement field originating from a dislocation at a point M(x, z) are

$$R_k(x,z) = \frac{1}{2i\pi}\sum_{\alpha=1}^{3} A_{k\alpha}D_\alpha \ln(x + p_\alpha z) + cc, \tag{8}$$

where the matrix $A_{k\alpha}$, the vector D_α and the quantities p_α, which are the roots of a sextic equation (Stroh 1958), depend on the elastic constants c_{ij}, on the direction of the dislocation and on the cut plane. It follows that at a point M′ ($X = \lambda x$, $Z = \lambda z$)

$$\frac{\partial R_k(\lambda x, \lambda z)}{\partial z} = -\frac{1}{2i\pi}\sum_{\alpha=1}^{3} A_{k\alpha}D_\alpha \frac{p_\alpha}{\lambda x + p_\alpha \lambda z} + cc = \frac{1}{\lambda}\frac{\partial R_k(x,z)}{\partial z}. \tag{9}$$

Equations (5) and (7) or (9) imply that multiplying $s_{\mathbf{g}}$ by λ results in an image $1/\lambda$ times closer to the geometrical projection of the dislocation line, a property which conforms to the remarks in § 3 about the similarity between images simulated at varied values of $s_{\mathbf{g}}$ (figures 2–5).

The property of similitude is better illustrated by means of the contour plots of equation (5) shown in figure 6. What happens is that, as $s_{\mathbf{g}}$ is decreased by a given factor, the locus of points where equation (5) is satisfied is homothetically expanded. This results in the magnification of the image overall features over the same factor (except of course for the image pseudoperiodicity and for the near-surface contrast which cannot be accounted for by the method of the generalized cross-section of Head *et al.* (1973)).

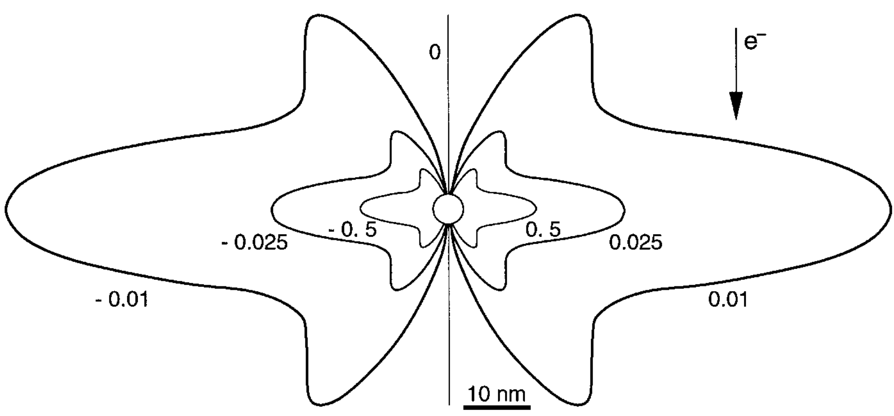

Figure 6. Contour maps of $s_{\mathbf{g}} + \partial(\mathbf{g}\cdot\mathbf{R})/\partial z = 0$ for $\mathbf{g} = 111$ and several values of $s_{\mathbf{g}}$ (e.g. 0, 0.01, 0.25 and 0.5 nm^{-1}), showing the property of similitude. The open circle symbolizes the crystal region around the dislocation core where the displacement gradients are so large that limited constructive interference, if any, can be expected (also this is the region where linear elasticity breaks down).

In elastically anisotropic conditions, finite components of $\mathbf{R}$ perpendicular to the Burgers vector superimpose on the axial displacement field of a screw dislocation, implying that, under $\mathbf{g} \cdot \mathbf{b} = 0$, the quantity $\mathbf{g} \cdot \mathbf{R}$ cannot be cancelled everywhere. As mentioned in § 1, this is the source of the sometimes pronounced *residual* contrast exhibited by dislocations imaged in near-Bragg conditions. Under such conditions, the image of a dislocation indeed consists of two components: the peak itself and a tail (Hirsch *et al.* 1965). The peak is generated in the region where the displacement varies sufficiently in an extinction distance $\xi_{\mathbf{g}}$ near the dislocation, in order to promote significant scattering. The tail, which can largely dominate the wholesale appearance of the dislocation image, originates from relatively small distortions and can be significantly influenced by elastic anisotropy (Head 1967). In the following, we examine the conditions of dislocation visibility–invisibility in weak-beam kinematical conditions, in which the tail effects are necessarily cancelled.

§ 5. Discussion

In § 5.1 we characterize diffraction in the vicinity of a dislocation in an anisotropic crystal and this is applied to predict the position of the image peak(s) and to discuss the invisibility criterion under weak-beam conditions in § 5.2 and 5.3 respectively. We make extensive use of cross-section contour maps of the gradient of $\mathbf{R}$ or of $\mathbf{g} \cdot \mathbf{R}$, whose usefulness has been recently demonstrated by Hemker (1997). It is worth recalling that, since the component of $\mathbf{R}$ parallel to the electron beam does not contribute to diffraction contrast, it is sufficient to consider the projection of the displacement field $\mathbf{R}$ on the y axis, which can be in turn decomposed into two components, $\mathbf{R}_{\parallel}$ and $\mathbf{R}_{\perp}$, parallel and perpendicular to the Burgers vector respectively.

5.1. *The implications of plots of $s_{\mathbf{g}}^{\mathrm{eff}}$*

One possible reason why, in β-CuZn, the contribution of anisotropic elasticity to the overall contrast properties of weak-beam images is not as pronounced as under dynamical conditions, could be that the anisotropy-related lattice rotations remain relatively modest in the core vicinity. At large values of $s_{\mathbf{g}}$, these rotations might in fact not be enough to contribute significantly to $\partial(\mathbf{g} \cdot \mathbf{R})/\partial z$ (equation (5)). We shall see at the end of § 5.2 that this explanation is in fact partly valid in moderately anisotropic crystals. As shown by figure 7, this is clearly not the case in β-brass for $\partial(\mathbf{R}_{\parallel})/\partial z$ and $\partial(\mathbf{R}_{\perp})/\partial z$ are actually of comparable spatial extension (figures 7 (*a*) and (*b*) respectively). Hence the lattice distortions which arise from isotropic elasticity (all included in $\mathbf{R}_{\parallel}$) or from anisotropic elasticity (the only contribution to $\mathbf{R}_{\perp}$) may well compensate for large deviations from Bragg conditions at comparable distances from the dislocation core. Figure 7 (*c*), which shows contour maps of $\partial(\mathbf{R}_{\parallel} + \mathbf{R}_{\perp})/\partial z$ projected along the [001] direction, indicates that the resultant gradient can be substantially modified by $\partial(\mathbf{R}_{\perp})/\partial z$.

The contribution of elastic anisotropy to the formation of the image is further illustrated in figure 8 where contour maps of the local lattice rotation $\partial(\mathbf{g} \cdot \mathbf{R})/\partial z$ are plotted for each of the most currently employed, fundamental reflections of the $[1\bar{1}0]$ zone axis. Selecting a reflection $\mathbf{g}$, at an angle θ from $\mathbf{b}$, is equivalent to superimposing the two gradients of displacement fields in varied relative weights (i.e. $g(\cos\theta\,\partial R_{\parallel}/\partial z + \sin\theta\,\partial R_{\perp}/\partial z)$). Depending upon the weight of $\partial(\mathbf{R}_{\parallel})/\partial z$ relative to $\partial(\mathbf{R}_{\perp})/\partial z$, contour maps show a large variety of shapes depending on the operating $\mathbf{g}$ vector in this selected section of the reciprocal plane. The fact that the lobes of

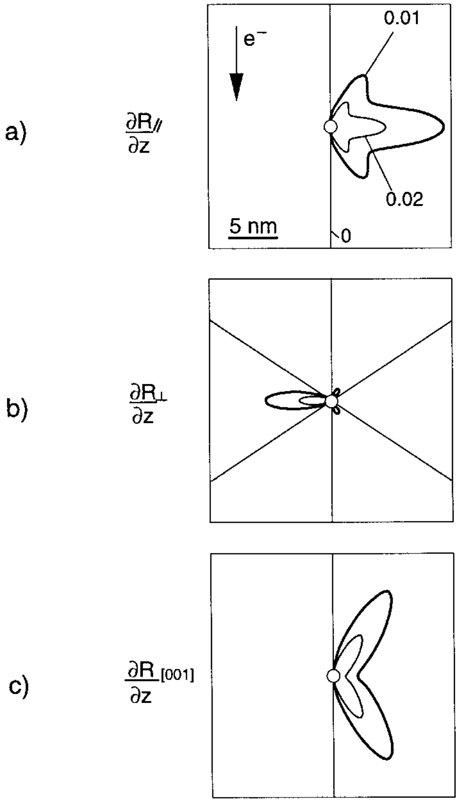

Figure 7. Contour maps of the gradient of the displacement field generated by a screw dislocation with Burgers vector [111] in β-brass as these can be evidenced in practice by projecting $\mathbf{R}$ onto different $\mathbf{g}$ vectors. These contour maps are displayed for three values of $\partial(\mathbf{g}\cdot\mathbf{R})/\partial z$, for example 0, 0.01 and 0.02 (straight lines, thin lines and thick lines respectively). (*a*) $\partial(\mathbf{R}_{\|})/\partial z$. (*b*) $\partial(\mathbf{R}_{\perp})/\partial z$. (*c*) Projection of $\partial(\mathbf{R})/\partial z$ along [001] in this particular combination of the two components, $\partial(\mathbf{R}_{\|})/\partial z$ still dominates but is markedly distorted by the superimposition of $\partial(\mathbf{R}_{\perp})/\partial z$.

$\partial(\mathbf{R}_{\|})/\partial z$ and of $\partial(\mathbf{R}_{\perp})/\partial z$ are located on either side of the median (figures 7 (*a*) and (*b*) respectively) is reflected by the various contour maps of $\partial(\mathbf{g}\cdot\mathbf{R})/\partial z$ in figure 8.

5.2. *The position of peak(s) of the dislocation image*

As mentioned earlier, since the closer to the dislocation the steeper is the gradient of $\varepsilon(\mathbf{r})$, *the volume of crystal* which is actually in Bragg condition, or sufficiently near this orientation for the diffracted signal to remain significant, becomes smaller upon increasing s_g. This property has the two well known conflicting implications that, as the deviation from the Bragg condition increases, the image resolution increases while the peak intensity decreases (as s_g^{-2}). A limitation arises in practice from the fact that not enough atoms are in position to scatter an electron wave constructively in the direction of the diffracted beam. One experimentally observes indeed that, upon increasing s_g, the weak-beam image of an otherwise visible defect fades away but there is no simple means to determine the smallest diffracting volume that can possibly generate a detectable signal. Accordingly, a further condition for a signal to emerge from the background of a weak-beam image is that the compensation for

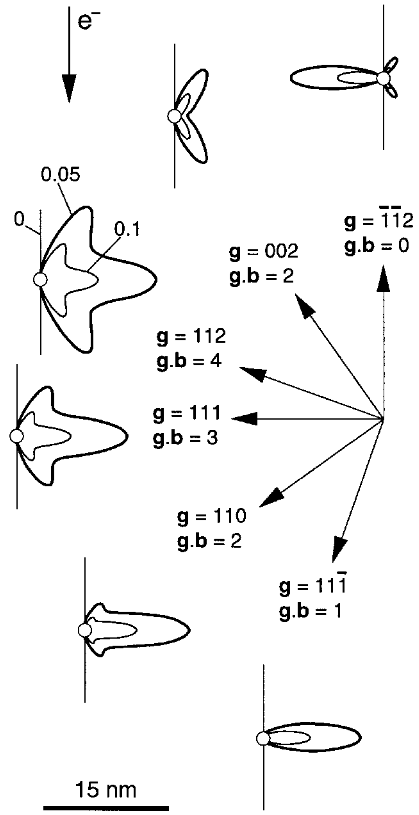

Figure 8. Contour maps for selected vectors $\mathbf{g}$ within the $[1\bar{1}0]$ zone axis, that is for a variety of combinations of $\partial(\mathbf{R}_{\parallel})/\partial z$ and $\partial(\mathbf{R}_{\perp})/\partial z$. Between $\mathbf{g} = 111$ and $\mathbf{g} = 112$, $\partial(\mathbf{R}_{\perp})/\partial z$ subtracts to $\partial(\mathbf{R}_{\parallel})/\partial z$ while these components are of the same sign for $\mathbf{g} = 110$ and $\mathbf{g} = 111$.

lattice rotation, as implied by equation (5), is satisfied over a finite fraction of column δz. The longer the length of contour map which is tangent to the beam, the brighter is the signal that emerges from the column under consideration. In terms of lattice rotation this defines portions of column where $\partial(\mathbf{g}\cdot\mathbf{R})/\partial z$ does not vary too rapidly, a description which is usually expressed by the additional condition that (Cockayne *et al.* 1969)

$$\frac{\partial^2(\mathbf{g}\cdot\mathbf{R})}{\partial z^2} = 0 \tag{10}$$

where equation (5) is satisfied (for a discussion of this question, see Cockayne (1972), Williams and Carter (1996) and Hemker (1997). Condition (10) indicates that $\mathbf{R}$ assumes an inflection but the extent over which $\mathbf{R}$ is stationary is actually unknown. Condition (10) thus cannot guarantee that the overall intensity which emerges from the corresponding column is sufficiently high that it gives rise to a detectable signal.

Graphically, locating the image peak is equivalent to finding the crystal column which, over the longest possible length, is tangent or near tangent to the contour map (figure 9). Onto the contour map of $\partial(\mathbf{g}\cdot\mathbf{R}_{\perp})/\partial z = -0.05\,\mathrm{nm}^{-1}$, we have superimposed in figure 9(a) the depth dependence of $\mathbf{R}_{\perp}$, but magnified by a

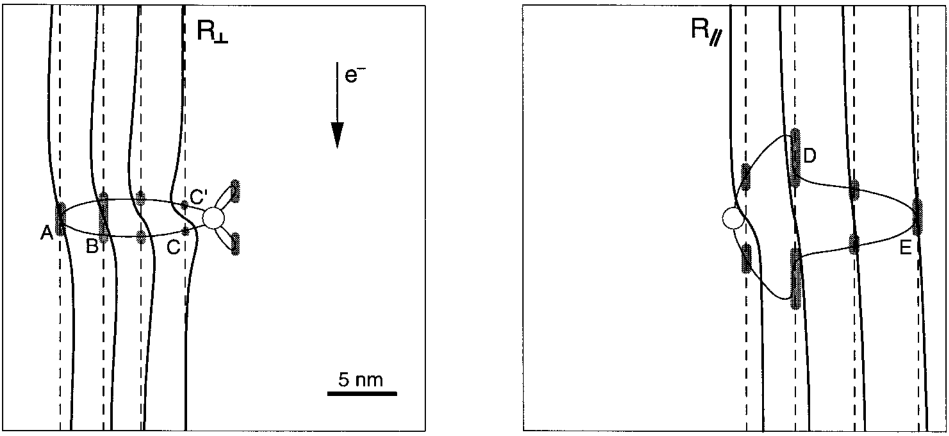

(a) (b)

Figure 9. The conditions of image formation based on the contour maps of equation (5) and on the depth dependence of the displacement field $\mathbf{R}$ along columns in the direction of the electron beam. The vertical broken lines embody the columns in which the displacements (thick inflected curves) are calculated. The grey strips schematize the crystal volumes where equations (5) and (10) are thought to be simultaneously satisfied. The intensity at the bottom of the column is expected to be roughly proportional to the length of the grey strips. (a) $\mathbf{g} = 1\bar{1}2$; $\mathbf{g}\cdot\mathbf{b} = 0$. For clarity, the displacement field $\mathbf{R}_\perp$ is multiplied by 50. (b) $\mathbf{g} = 111$; $\mathbf{g}\cdot\mathbf{b} = 2$. The axial displacement field $\mathbf{R}_\parallel$ is multiplied by 10 and projected onto the plane of the figure.

factor of 50. For simplicity, we just consider the crystal slab that contains the large horizontal lobe and we note that, out of the three inflection points of $\mathbf{R}_\perp$ associated with each column, it is enough to focus on that located in the near vicinity of the lobe. As one can see, there is in principle one single location where conditions (5) and (10) are simultaneously satisfied, for example at the left-hand side tip of $\partial(\mathbf{g}\cdot\mathbf{R}_\perp)/\partial z = -0.05\,\mathrm{nm}^{-1}$ (A in figure 9(a)). What occurs is that, while the inflection point of $\mathbf{R}_\perp$ remains at the same depth as that of the dislocation core†, condition (5) is actually satisfied twice in each column, except of course for the degeneracy at A. Close to the dislocation such as at C–C′, the two points where the lobe intersects the column are separated by a region of rapidly varying gradient of $\mathbf{R}_\perp$. Hence, the total length over which $\partial^2(\mathbf{g}\cdot\mathbf{R}_\perp)/\partial z^2 \approx 0$ is satisfied in the vicinity of the lobe along this column is significantly shorter than at A for instance; it shows limited overlap, if any, with the volumes around C and C′ where condition (5) is fulfilled. The signal which emerges from this column is expected to be less than the signal emerging from the column containing A. Figure 9(a) suggests in addition that there is a column located at B, in between A and C, where the quantity $s_\mathbf{g} + \mathbf{g}\cdot\partial\mathbf{R}_\perp/\partial z$ is *approximately* cancelled over a length δz and yet longer than for A. It is from this column that the emerging signal should peak, hence explaining graphically why conditions (5) and (10) do not predict precisely the position of the intensity maximum (Cockayne 1972, Williams and Carter 1996, Hemker 1997).

The fact that condition (5) need not be satisfied rigorously in order to give rise to a finite signal arises in particular from the angular dependence of the structure factor

† This does not apply to dissociated dislocations in which case the height of the inflection point depends on the orientation of the habit plane(s) of the partial.

of the operating reflection and from the fact that the incident beam comprises all incidences within the range of deviation parameters $[s_{\mathbf{g}} - \delta s_{\mathbf{g}}, s_{\mathbf{g}} + \delta s_{\mathbf{g}}]$. Under these conditions, close to the volume where conditions (5) and (10) are satisfied for the deviation $s_{\mathbf{g}}$, there is another region where the variation of $\mathbf{g} \cdot \partial \mathbf{R}/\partial z$ is still smooth and which is in Bragg orientation for $s_{\mathbf{g}} + \delta s_{\mathbf{g}}$. For this reason, conditions (5) and (10) had rather be written

$$s_{\mathbf{g}} + \frac{\partial(\mathbf{g} \cdot \mathbf{R})}{\partial z} \in [-\delta s_{\mathbf{g}}, \delta s_{\mathbf{g}}], \tag{11}$$

$$\frac{\partial^2 \mathbf{g} \cdot \mathbf{R}}{\partial z^2} \approx 0. \tag{12}$$

The consequence of this is embodied in figure 9 under the form of grey strips which represent (but very roughly) which regions of the crystal the image peak is likely to originate from. Incidentally, it should be noted that reducing the beam divergence should narrow the dislocation image, decrease its intensity and move it away from the dislocation line towards the tip of the contour map (for a discussion of the effects of beam divergence upon the properties of a dislocation image under weak-beam conditions, see Meng *et al.* (1997)).

5.3. *The conditions of dislocation visibility*

From the above considerations one can understand why the invisibility criterion is actually applicable under weak beam in β-CuZn. Despite the similar extent of the lobes of the gradients of $\mathbf{R}_{\parallel}$ and $\mathbf{R}_{\perp}$ (figures 7 (*a*) and (*b*) respectively), the near invisibility of the screw dislocation under $\mathbf{g} \cdot \mathbf{b} = 0$ comes from differences in the column lengths over which conditions (11) and (12) are fulfilled. Given a range of deviation from Bragg conditions $s_{\mathbf{g}} \pm \delta s_{\mathbf{g}}$, it is indeed clear that, although this occurs on two separate segments, the length over which conditions (11) and (12) are satisfied is longer in figure 9 (*b*) than in figure 9 (*a*). In other words, whereas a dislocation peak can be conjectured from both figures 9 (*a*) and (*b*), that corresponding to $\mathbf{g} \cdot \mathbf{b} = 0$ is expected to be weaker than that obtained when $\mathbf{g}$ is taken parallel to $\mathbf{R}_{\parallel}$. In the latter case, the above reasoning predicts in addition that the image is twofold (figure 9 (*b*)). One peak originates from column D and is relatively intense, as discussed above. The second peak, which emerges in the vicinity of column E, is expected to be fainter (the length of the diffracting path is similar to that at A in figure 9 (*a*)). Note that figure 9 (*a*) suggests that a second image peak should arise from the vertical tangents to the oblique lobes and that this peak should exhibit about the same intensity as its companion though somewhat narrower. Figure 10 shows selected contour maps superimposed on the corresponding magnified simulated images. Clearly, the above graphical considerations are in good qualitative agreement with the simulated images. Observed differences arise from a number of causes including the effects of depth oscillations as well as the fact that the graphical method cannot take into account that both the modulus of $\mathbf{g}$ and the structure factor of the reflection differ from one image to the next. In the same vein as for the discussion on figure 9, the change in the shape of the contour map of $\partial(\mathbf{g} \cdot \mathbf{R})/\partial z$ as θ is varied and, in particular, the narrowing of its vertical extension (see figure 8, from $\mathbf{g} = 112$, then to 111, 110 and eventually to $11\bar{1}$) suggests that the main peak of the dislocation image, that is that associated to the vertical pair of segments of the contour maps, should weaken as the angle between $\mathbf{b}$ and $\mathbf{g}$ is increased.

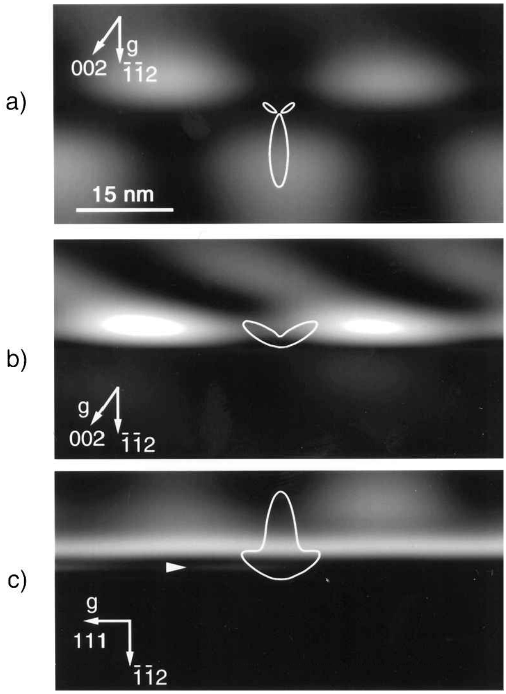

Figure 10. A superimposition of the simulated images (prints are overexposed) and of the contour maps of equation (5) presented under the same scale. In fact the habit plane of the contour map would be edge on (see figure 1). (*a*) $\mathbf{g} = \bar{1}\bar{1}2$; that is $\mathbf{g}\cdot\mathbf{b} = 0$; $s_{\mathbf{g}} = 0.1\,\mathrm{nm}^{-1}$. The asymmetry of the image is roughly accounted for (its most extended lobe is indeed directed downwards, towards the most elongated lobe of the contour map). The line of no contrast corresponds to the portion of the contour map close to the dislocation core, where the formalism is in fact not applicable (open circles in figures 6 and 7). That the brightnesses of the upper and of the lower lobes are about the same is consistent with the fact that the total lengths of contour map tangent to the beam (figure 9) are roughly the same on both sides of the dislocation line. However, why the upper image lobes appear more extended than expected from the contour map is unclear. (*b*) $\mathbf{g} = 002$; $\mathbf{g}\cdot\mathbf{b} = 2$; $s_{\mathbf{g}} = 0.1\,\mathrm{nm}^{-1}$. From the contour maps, one expects that the portions of column in Bragg conditions are longer in this case than in figure 10(*a*), resulting in brighter image lobes, as is the case in the simulation. Note also that the extension of the lobe perpendicular to the dislocation line is less for this $\mathbf{g}$ vector than for $\mathbf{g} = \bar{1}\bar{1}2$ (figure 10(*a*)); in this case, the consistency between the contour map and the image is fair. (*c*) $\mathbf{g} = 111$; $s_{\mathbf{g}} = 0.1\,\mathrm{nm}^{-1}$; the position of the image peak coincides rather satisfactorily with the shape of the contour map and the presence of the upper, fainter intensity lobes can be expected from this shape too. There is, however, a question as to the origin of the fainter line (arrow).

Finally we address the influence of the 'magnitude' of elastic anisotropy. Let us recall that a given value of the Zener factor A can be obtained from a large (in fact infinite) variety of combinations of the three elastic constants of a cubic crystal. Hence, in order to explore the influence of anisotropy, it is in principle necessary to refer to a second elastic coefficient, which can be taken as B (Head 1967) or as M (Saada and Veyssière 1992), and to explore a range of physically sound values (Head 1967). This is in fact not useful in the present general context and we have limited our analysis to comparing between hypothetical crystals whose Zener factors vary

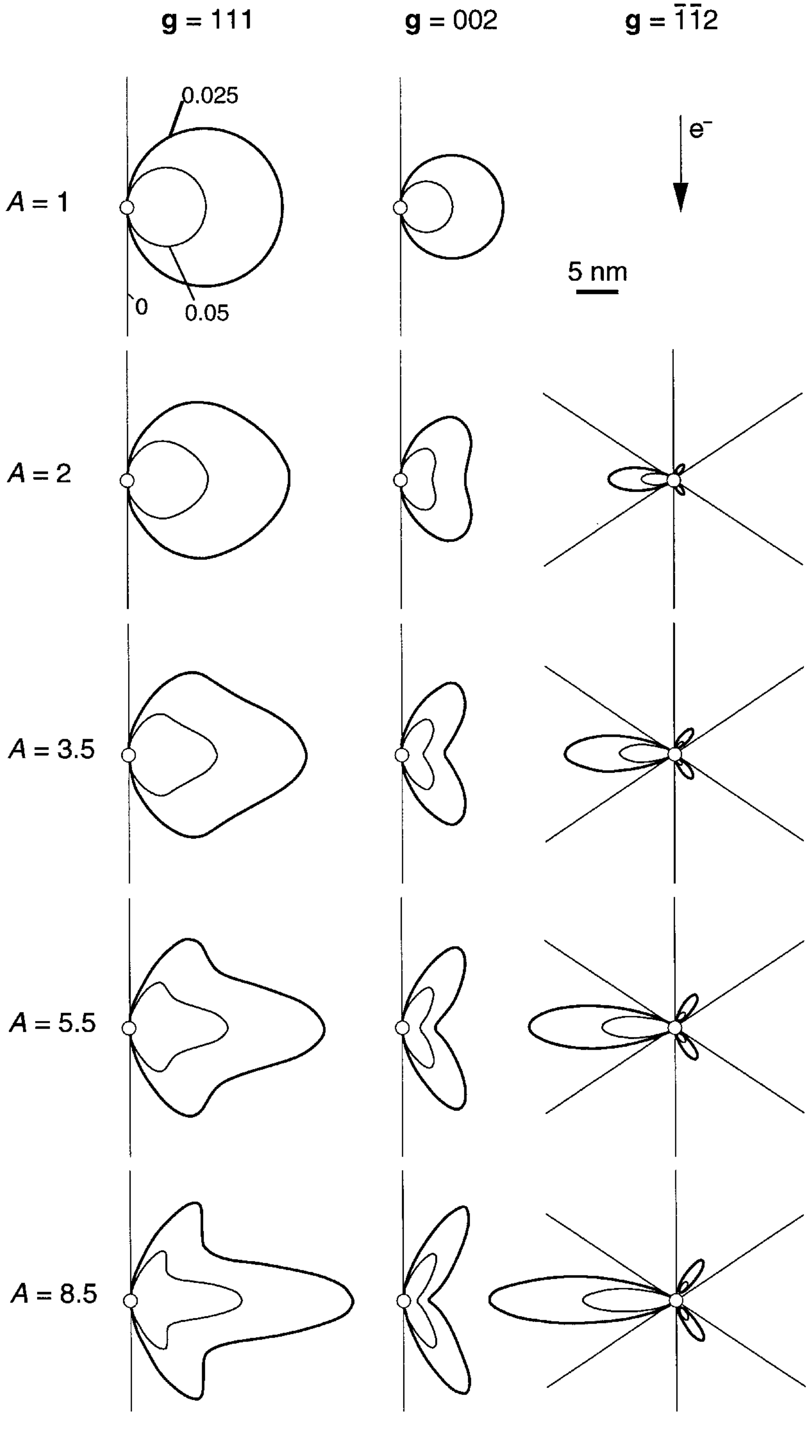

Figure 11. Effects of the degree of elastic anisotropy of a model crystal on the extension and the shape of contour maps for various sections of the displacement field of a screw dislocation, as determined by three selected diffraction vectors, for three values of $s_{\mathbf{g}}$ (0, 0.025 and 0.05 nm^{-1}). The increasing influence of $\mathbf{R}_{\perp}$ on the displacement field with increasing elastic anisotropy is visible regardless of the operating $\mathbf{g}$ vector.

between the isotropic case and that of β-CuZn, which covers quite a large range of Zener factors. In figure 11, the contours maps in the five crystals are plotted when imaged under the 111, 002 and $\bar{1}\bar{1}2$ reflections (002 mixes up the two components of the displacement field). As the anisotropy is decreased, the lobe of $\partial(\mathbf{R}_{\parallel})/\partial z$ is so much more predominant that of $\partial(\mathbf{R}_{\perp})/\partial z$ that the operating reflection is no longer capable of favouring the latter at the expense of the former. In moderately anisotropic crystals, the reason for the applicability of the $\mathbf{g}\cdot\mathbf{b} = 0$ criterion is therefore that elastic anisotropy tends to act as a slight perturbation of the isotropic solution which, at the level of lattice rotation required by the weak-beam technique, is not sufficient to modify the image enough for it to differ significantly from the 'elastically isotropic' image.

§ 5. Conclusion

By means of a suitable procedure of image display, the contrast properties of weak-beam images simulated under non-equivalent conditions can be confronted in the same way as this is done in practice. The origin of the applicability of the $\mathbf{g}\cdot\mathbf{b} = 0$ invisibility criterion in β-CuZn, which is markedly anisotropic, depends on the detail of the strain field of the dislocation and on the conditions of image formation specific to this imaging mode. By contrast, in moderately anisotropic crystals, this is simply the result of the relatively modest magnitude of the perturbation brought about by anisotropy. We have confirmed that methods that would rely on the application of simplistic criteria for image formation are not directly adequate to predict the position of the image peaks. When the physical origin of contrast formation is understood, the criteria can be modified in order to depict the actual situation more closely; yet a full analysis of dislocation images requires the support of image simulations.

Acknowledgement

Dr Robin Schäublin is gratefully acknowledged for very constructive discussions and for having provided us with the modified program Cufour that takes our requests on the procedure of determination of the exposure time into account.

References

Baluc, N., and Schäublin, R., 1996, *Phil. Mag.* A, **74**, 113.
Cockayne, D. J. H., 1972, *Z. Naturf.*, (a), **27**, 452.
Cockayne, D. J. H., Ray, I. L. F., and Whelan, M. J., 1969, *Phil. Mag.*, **20**, 1265.
Eshelby, J. D., Read, W. T., and Shockley, W., 1970, *Phil. Mag.*, **21**, 931.
Head, A. K., 1967, *Aust. J. Phys.*, **20**, 557.
Head, A. K., Humble, P., Clareborough, L. M., Morton, A. J., and Forwood, C. T., 1973, *Computed Electron Micrographs and Defect Identification* (Amsterdam: North-Holland).
Hemker, K. J., 1997, *Phil. Mag.* A, **76**, 241.
Hemker, K. J., and Mills, M. J., 1993, *Phil. Mag.* A, **68**, 305.
Hirsch, P. B., Howie, A., Nicholson, R. B., Pashley, D. W., and Whelan, M. J., 1960, *Electron Microscopy of Thin Crystals* (London: Butterworth).
Lazarus, P., 1948, *Phys. Rev.*, **74**, 1726; 1949, *ibid.* **76**, 547.
Meng, X., Schäublin, R., and Stobbs, W. M., 1997, *Phil. Mag.* A, **75**, 179.
Saada, G., and Veyssière, P., 1992. *Phys. Stat. sol.* (b), **172**, 309.
Saka, H., 1984, *Phil. Mag.* A, **49**, 327.
Schäublin, R., and Stadelman, P., 1993, *Mater. Sci. Engng*, **A164**, 373.
Stroh, A. N., 1958, *Phil. Mag.*, **3**, 625.
Williams, D. B., and Carter, C. B., 1996, *Transmission Electron Microscopy: A Textbook for Materials Science* (New York: Plenum), p. 428.